

## RESEARCH ARTICLE

# Core-passivation: A concept for stable core-shell nanoparticles in aqueous electrocatalysis

Daniel Göhl<sup>1</sup> | Paul Paciok<sup>2</sup> | Zhenshu Wang<sup>3</sup> | Jin Soo Kang<sup>3</sup> | Marc Heggen<sup>2</sup> | Karl J. J. Mayrhofer<sup>4,5</sup> | Yuriy Román-Leshkov<sup>3</sup> | Marc Ledendecker<sup>1,6</sup>

<sup>1</sup>Department of Chemistry, Ernst-Berl-Institut für Technische und Makromolekulare Chemie, Technical University of Darmstadt, Darmstadt, Germany

<sup>2</sup>Ernst Ruska-Centre for Microscopy and Spectroscopy with Electrons and Peter Grünberg Institute, Forschungszentrum Jülich GmbH, Jülich, Germany

<sup>3</sup>Department of Chemical Engineering, Massachusetts Institute of Technology, Cambridge, Massachusetts, USA

<sup>4</sup>Helmholtz-Institute Erlangen-Nürnberg for Renewable Energy, Forschungszentrum Jülich GmbH, Erlangen, Germany

<sup>5</sup>Department of Chemical and Biological Engineering, Friedrich-Alexander-Universität Erlangen-Nürnberg, Erlangen, Germany

<sup>6</sup>Professorship Sustainable Energy Materials, Technical University Munich, Straubing, Germany

## Correspondence

Daniel Göhl, Department of Chemistry, Ernst-Berl-Institut für Technische und Makromolekulare Chemie, Technical University of Darmstadt, 64287 Darmstadt, Germany.

Email: [daniel.goehl@tu-darmstadt.de](mailto:daniel.goehl@tu-darmstadt.de)

Yuriy Román-Leshkov, Department of Chemical Engineering, Massachusetts Institute of Technology, Cambridge, MA 02139, USA.

Email: [yroman@mit.edu](mailto:yroman@mit.edu)

Marc Ledendecker, Campus Straubing for Biotechnology and Sustainability, Technical University Munich, 94315 Straubing, Germany.

Email: [marc.ledendecker@tum.de](mailto:marc.ledendecker@tum.de)

## Funding information

Federal Ministry of Education and Research; SynKat, Grant/Award Number: 03XP0265; Germany in the framework of POREForm, Grant/Award Number: 003ETB027G

## Abstract

The stability of nanoparticles is a major challenge in thermal and electrocatalysis. This is especially true for core-shell nanoparticles where only a few monolayers of noble metal protect the usually non-noble core material. In this work, we utilize the practical nobility concept to engineer stable core-shell nanoparticles with a self-passivating core material. Specifically, tantalum carbide as core material in combination with a 1–3 monolayer thick platinum shell exhibits exceptional stability in aqueous media. The core-shell catalyst shows no sign of structural changes after 10,000 degradation cycles up to 1.0 V<sub>RHE</sub>. Due to the efficient passivation of tantalum carbide at the solid/liquid interface, the dissolution reduces by a factor of eight compared to bare Pt. Our findings confirm that passivating core materials are highly beneficial for the stabilization of core-shell nanomaterials in aqueous media. They open up new ways for the rational design of cost-efficient but stable non-noble core – platinum shell nanoparticles where harsh, oxidizing conditions are employed.

## KEYWORDS

electrocatalysts, fuel cell, oxygen reduction reaction, stability

This is an open access article under the terms of the [Creative Commons Attribution](https://creativecommons.org/licenses/by/4.0/) License, which permits use, distribution and reproduction in any medium, provided the original work is properly cited.

© 2023 The Authors. *Nano Select* published by Wiley-VCH GmbH.

## 1 | INTRODUCTION

Nanoparticles have attracted considerable attention in thermal and electrocatalysis due to their unique properties compared to their bulk phase such as their high specific surface area, the high number of undercoordinated atoms, strain, or quantum effects.<sup>[1–3]</sup> As the nanoparticle size decreases, the surface energy increases making the particles prone to destabilization.<sup>[4,5]</sup> Polymer electrolyte membrane fuel cells use platinum catalysts that are alloyed with transition metals such as Co, Ni, Mo, Fe, or Cu.<sup>[6–8]</sup> These elements, however, are neither thermodynamically, nor kinetically stable in the acidic environment at oxygen reduction relevant conditions.<sup>[9]</sup> We recently demonstrated that Ni and Mo dissolution takes place even at open circuit potential for octahedral-shaped Pt<sub>3</sub>Ni nanoparticles doped with Mo.<sup>[10]</sup> The dissolution continues at higher potentials until a protecting Pt-shell and quasi-core-shell particles are formed. The same holds for a variety of alloyed nanoparticles.<sup>[6,11,12]</sup> One strategy to stabilize the surface lies in the introduction of other noble metals such as Au,<sup>[13]</sup> Ir,<sup>[14]</sup> Ru,<sup>[15]</sup> or Pd.<sup>[16]</sup> The synthesized core-shell particles exhibit higher specific area normalized activities (SA) compared to bare platinum.<sup>[17–19]</sup> For Pt/Au, additional stabilization of Pt was found.<sup>[19,20]</sup> Despite the increased stabilization, however, substituting a noble metal with another noble metal leads only to a marginal cost reduction<sup>[21,22]</sup> while strategies to overcome these limitations are needed. Even noble metals such as Pd dissolve and lead to severe membrane poisoning if not treated beforehand.<sup>[22]</sup> From a practical point of view, cost-efficient materials have to be found that can withstand the harsh conditions and offer sufficient conductivity. Leaving thermodynamic stabilization aside, the practical nobility is, next to the thermodynamic nobility, a useful concept to target stable materials that can be used to support noble metals such as Pt. Electrochemical equilibrium diagrams, usually termed as “Pourbaix-diagrams” bring out the passivation effect of various, usually non-noble metals.<sup>[9]</sup> In a previous work on thin films, substrate degradation was completely inhibited by potential-triggered surface passivation healing out defects in the overlaying Pt film.<sup>[23]</sup> However, the synthesis and applicability to nanoparticle systems are highly challenging as high temperatures are necessary that habitually lead to sintering and agglomeration. In the here presented study, we take advantage of the practical nobility concept and extend our work to applicable nanoparticulate systems with a large, total surface area. This is shown exemplarily for tantalum carbide as core material to support platinum followed by a detailed examination of its electrochemical stability. Transition metal carbides are ideal core candidates as they are immiscible with noble metals,<sup>[24]</sup> exhibit a high interfacial binding

energy with Pt,<sup>[25]</sup> and experience enthalpic stabilization through the partial covalent character of the metal-carbon bond.<sup>[26]</sup> We synthesized Pt on TaC core-shell nanoparticles via a reversed microemulsion synthesis route with varying monolayer (ML) thicknesses.<sup>[27]</sup> To elaborate on the stability, we followed the degradation by in situ and ex situ characterization methods. Specifically, in situ electrochemical flow cell measurements were used to track potential dependent dissolution of noble and non-noble elements. By identical location high resolution scanning transmission electron microscopy (IL-HR-STEM) paired with energy-dispersive X-ray spectroscopy (EDX), we follow the degradation trajectories and elemental composition after accelerated stress tests. These self-passivating core-shell structures achieve improved dissolution stability and reduced noble metal loading compared to state-of-the-art catalysts for electrochemical application.

## 2 | EXPERIMENTAL SECTION/METHODS

Detailed experimental procedures can be found in the [Supporting Information](#).

## 3 | RESULTS AND DISCUSSION

First, two sets of catalyst nanoparticles were synthesized, one with a nominal 1.2 monolayer- (Pt<sub>1.2ML</sub>/TaC) and 2.6 monolayer- (Pt<sub>2.6ML</sub>/TaC) Pt coverage on TaC.<sup>[28]</sup> The synthesis procedure followed a modified reversed microemulsion (RME) route described by Hunt et al and is shown in Figure 1A.<sup>[27,28]</sup> First, tantalum oxide nanoparticles were synthesized by hydrolysis followed by the addition of a Pt-precursor. A silica shell was used to encapsulate the synthesized nanoparticles that allowed for thermal carburization in H<sub>2</sub> and CH<sub>4</sub> up to 1100°C while actively suppressing sintering and agglomeration. The full temperature profile is shown in Figure S1. The protecting SiO<sub>2</sub> shell was removed by HF in ethanol and the particles were supported on carbon black. The detailed synthetic procedure, further physico-chemical characterization, and discussion of the synthesis can be found in the SI (Figures S2–S4). The powder X-ray diffractogram (XRD) revealed the successful formation of TaC<sub>fcc</sub>, with minimal contribution from PtTa<sub>2</sub>, confirming the predicted immiscibility of Pt and TaC (Figure 1E). Reflections of Pt could not be observed indicating that Pt is in close contact with Ta and that the reflexes of potentially formed Pt-nanoparticles are too weak to be detected. The diffraction pattern's shape is consistent with the size distribution observed through TEM (as shown in Figure S4). The presence of defects

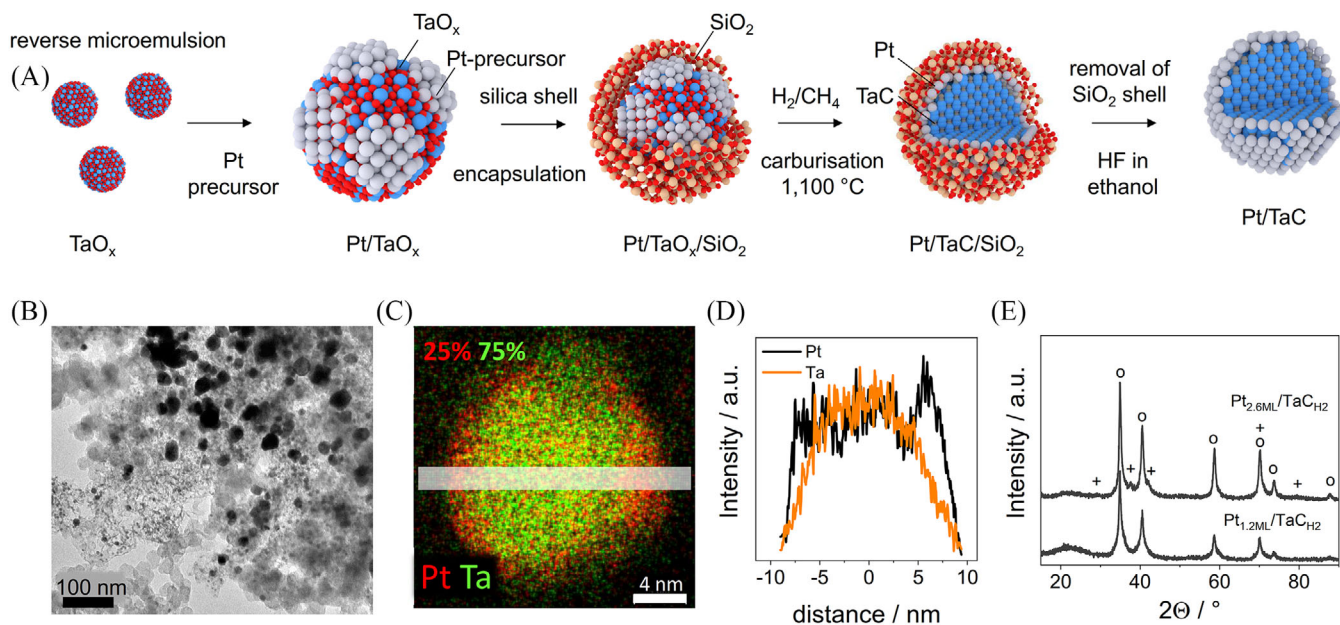


**FIGURE 1** A, Schematic overview of the applied synthesis using a solid surfactant to obtain Pt/TaC core-shell particles. B, Transmission electron microscopic image over a large area showing both small particles and large aggregates. C, High-resolution EDX mapping and line scan (D) of a single particle confirming the core-shell structure. E, PXRD diffractograms of  $\text{Pt}_{2.6\text{ML}}/\text{TaC}$  and  $\text{Pt}_{1.2\text{ML}}/\text{TaC}$ , o: TaC, +:  $\text{PtTa}_2$ . a.u., arbitrary units

in the crystal structure may also have contributed to the observed peak shape. The core-shell structure displays regular shell defects that were expected as complete carburization of  $\text{TaO}_x$  due to its oxophilic nature remains highly challenging. The general core-shell structure was confirmed via (S)TEM measurements (Figure 1B–D). The mean crystallite size for  $\text{Pt}_{2.6\text{ML}}/\text{TaC}$  and  $\text{Pt}_{1.2\text{ML}}/\text{TaC}$  was calculated by Scherrer's equation to be  $12.3 \pm 1.4$  nm and  $10.8 \pm 0.6$  nm, respectively, and compared to the particle size distribution obtained from electron microscopy (Figure S4d).<sup>[29,30]</sup> From the average particle size and the elemental composition from inductively coupled plasma mass spectrometry (ICP-MS) and (S)TEM/EDX measurements, the average shell thickness was estimated to be 1.2 ML and 2.6 ML.

As a first indication of stability, both catalysts were examined by in situ scanning flow cell (SFC) measurements that were coupled to inductively coupled plasma mass spectrometry. These measurements allow for measuring the simultaneous potential dependent dissolution of each element. To obtain a clear image of the potential-dependent dissolution, a cyclic voltammogram was recorded from 0.0 to  $1.5 V_{\text{RHE}}$  with a scan rate of  $2 \text{ mV s}^{-1}$  (Figure 2A) in 0.1 M  $\text{HClO}_4$ . The metal dissolution was recorded concomitantly with the potential and normalized to the electrochemically active surface area (ECSA, Figure 2A middle, and lower panel).<sup>[31]</sup> As a reference, a bare TaC thin film, a polycrystalline Pt film, and 10 nm  $\text{Pt}_3\text{NiMo}$  octahedra supported on Vulcan<sup>[10]</sup>

were measured under the same conditions (Figure 2B). For all Pt-containing materials, Pt-oxidation above  $1.0 V_{\text{RHE}}$  results in dissolution that is getting more pronounced when the platinum oxide is reduced back to Pt(0) during the cathodic scan near  $0.7 V_{\text{RHE}}$ .<sup>[32]</sup> For  $\text{Pt}_{2.6\text{ML}}/\text{TaC}$ , the ratio of cathodic to anodic dissolution decreased to 3.1 compared to 6.5 for  $\text{Pt}_{\text{bulk}}$ . This indicates either stabilization of the Pt shell by the TaC core during reduction or a destabilization at oxidative potentials above  $1.05 V_{\text{RHE}}$ . The overall reduced amount of dissolved platinum for  $\text{Pt}_{2.6\text{ML}}/\text{TaC}$  suggests rather a successful stabilization by the Pt/TaC interaction. For bare TaC, an oxidative current peak accompanied by Ta dissolution was observed above ca.  $0.75 V_{\text{RHE}}$  which is consistent with previous reports.<sup>[26]</sup> The Pt/TaC core-shell system exhibits a markedly different Ta dissolution profile compared to the bare carbide. For  $\text{Pt}_{2.6\text{ML}}/\text{TaC}$ , a first small dissolution peak upon electrolyte contact was observed at  $0.0 V_{\text{RHE}}$  originating presumably from the Pt-catalyzed reduction of surface (hydr-)oxides and vanishes in consecutive cycles (Figure S5). Ta oxidation or dissolution was not observed around the oxidation potential of TaC. As part of the TaC surface is not covered by Pt (Figure 1B and Figure S3), the missing oxidation peak indicates efficient surface passivation already at ambient or open circuit conditions. This facilitated oxidation was previously observed for Pt/WTiC core-shell nanoparticles where Pt catalyzed the oxidation of exposed carbide cores upon contact with air.<sup>[33]</sup> The difference in dissolution is strong evidence that exposed carbide fractions heal out by

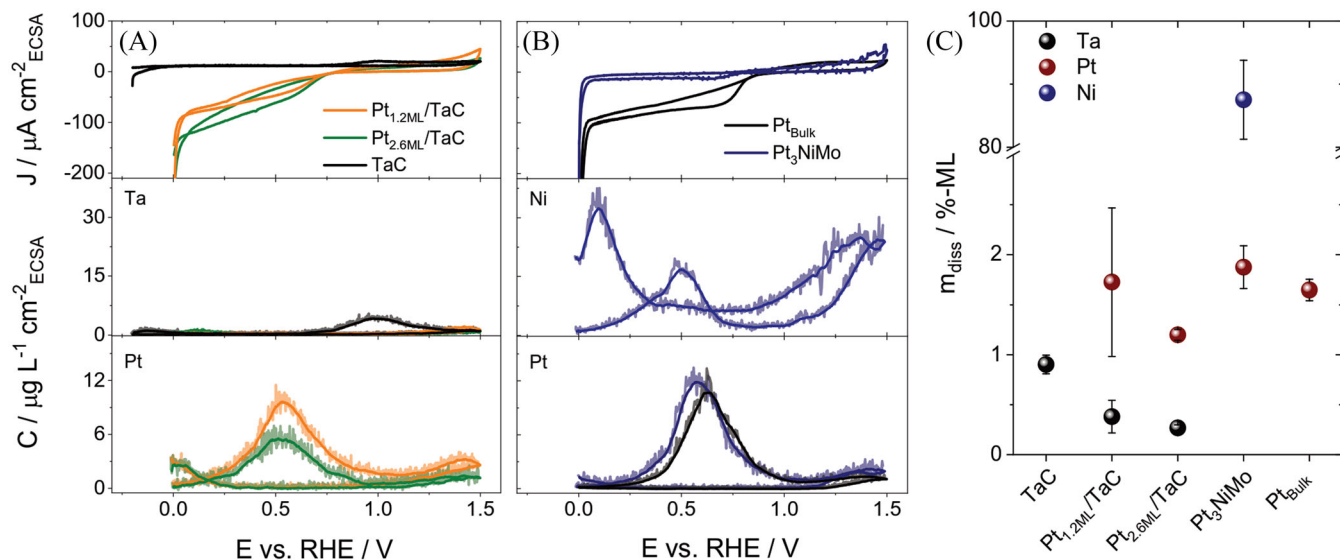


**FIGURE 2** A, Cyclic voltammogram and the corresponding Ta and Pt dissolution profiles of a bare TaC film, Pt<sub>1.2ML</sub>/TaC, and Pt<sub>2.6ML</sub>/TaC, B, cyclic voltammogram and the corresponding Ni and Pt dissolution profiles of polycrystalline Pt and 10 nm Pt<sub>3</sub>NiMo octahedra during one cycle between 0.0 V<sub>RHE</sub> (−0.2 V<sub>RHE</sub> for TaC) and 1.5 V<sub>RHE</sub> at 2 mV s<sup>−1</sup> in Ar-sat. 0.1 M HClO<sub>4</sub>. C, The corresponding total dissolution amounts during experiments are shown in (A) and (B). All currents and dissolution amounts or concentrations were normalized to the ECSA

forming insoluble surface oxides and prevent further core dissolution. Further oxidation and Ta dissolution were only observed concomitantly to oxidative Pt dissolution.

A clear indication of the exceptional stability of Ta is given by the missing Ta dissolution when Pt is reduced and dissolved. This is in strong contrast to, for example, Ni-core dissolution in Pt<sub>3</sub>NiMo. First, the dissolution peak above 0.0 V<sub>RHE</sub> at the beginning of the experiment is much more pronounced originating from Ni oxidation in the surface layers.<sup>[9]</sup> Then, Ni dissolution occurs concomitantly to both, oxidative and reductive Pt dissolution and no passivation was observed. In total, Ni dissolution is by a factor of 100 larger compared to Ta dissolution (Figure 2C).

To elaborate further on the stability, 1000 cycles between 0.4 and 1.0 V<sub>RHE</sub> with a scan rate of 1 V s<sup>−1</sup> were conducted while monitoring the dissolution via operando SFC-ICP-MS measurements. Figure 3A shows the dissolution profiles of Pt and Ta upon contacting the working electrode and during the AST. The first contact dissolution peak results from transient dissolution when platinum oxide is reduced or when non-stabilized Pt and Ta-surface atoms are dissolved. In total, the dissolution ranges between 0.8% (Pt) and 0.1% (Ta) of a monolayer upon contacting and declines rapidly. A second dissolution peak occurs upon starting the potential cycling and the AST. This results on the one hand from a forced reduction of PtO<sub>x</sub> at 0.0 V<sub>RHE</sub> and on the other hand, from further oxidation and dissolution of native, non-stabilized TaO<sub>x</sub>H<sub>y</sub> species.<sup>[33]</sup> As TaC is passivating strongly, the dissolution of both, Ta and Pt level off fast. To obtain an estimation of the lifetime of the catalyst, the dissolution amounts were integrated

over time (Figure 3B,C). During the course of the experiment, around 4% of one monolayer (% ML) of Pt and 0.5% ML of Ta dissolved. Further calculation details on the translation of concentration into monolayers can be found in the SI, Equations S6 to S8. Most dissolution takes place during the first cycles, as the dissolution decreases to 0.08 and 0.01% ML for Pt and Ta, respectively, over the last 100 cycles. These values demonstrate that TaC is even more dissolution-stable than Pt because of its surface oxide layer. This is supported by XPS measurements after 10,800 cycles between 0.4 and 1.0 (AST-1.0), where an oxide fraction of 86% and a carbide fraction of 14% were observed (Figure 3D). In comparison, the non-noble metal dissolution for Pt<sub>3</sub>Ni-Mo is much more pronounced (Figure 3A). During the last 100 cycles, Ni dissolution is by a factor of six higher compared to Pt and Ta dissolution added together. Our results clearly demonstrate that the use of passivating TaC and its high stability is an enormous improvement to other core-shell systems employing non-noble elements.<sup>[33]</sup>

IL-HR-STEM images and EDX maps were recorded in order to monitor the structural and morphological evolution of single core-shell particles prior to and after AST-1.0, Figure 3E,F, Figure S6). Despite parts of the TaC surface are not covered by Pt (white arrows Figure 3E), the core-shell structure is retained over 10,000 potential cycles and the shell defects remained comparable in size. The overall elemental composition (23% Pt, 77% TaC) only changed marginally within the range of the measurement error (22% Pt, 78% TaC), accentuating the high elemental stability. Restructuring or sintering was not observed. Possible

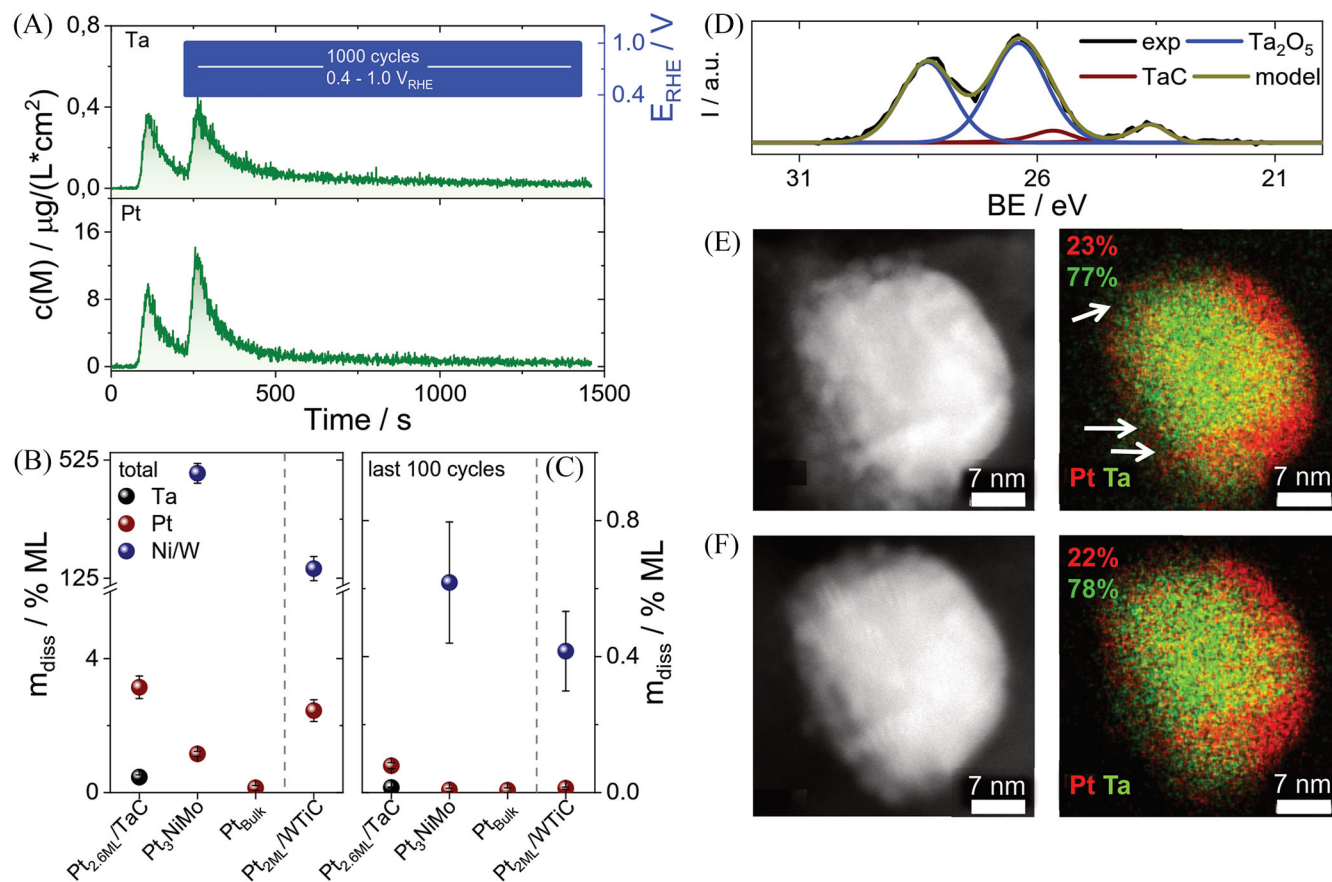


**FIGURE 3** A, Dissolution profiles of Ta/Ni and Pt for Pt<sub>2.6ML</sub>/TaC, Pt<sub>3</sub>Ni-Mo, and Pt<sub>Bulk</sub> upon cycling 1000 times between 0.4 and 1.0 V<sub>RHE</sub> at 1 V s<sup>-1</sup> in Ar-sat. 0.1 M HClO<sub>4</sub>. For a better comparison, the inset shows the last 150–200 seconds with a larger magnification. The corresponding total dissolved amounts during (B) the complete experiment, and (C) during the last 100 cycles together with values for a reference Pt bulk sample, carbon-supported Pt<sub>3</sub>NiMo octahedra with dp = 10 nm and Pt<sub>2ML</sub>/TiWC.<sup>[33]</sup> D, Ta 4f level XPS spectrum of Pt<sub>2.6ML</sub>/TaC after 10,800 cycles between 0.4 and 1.0 V<sub>RHE</sub> at 1 V s<sup>-1</sup> in Ar-sat. 0.1 M HClO<sub>4</sub>. Identical location STEM images and corresponding EDX elemental maps of Pt<sub>2.6ML</sub>/TaC (E) before and (F) after AST-1.0

reasons lie in (1) the immiscibility of Pt and transition metal carbides,<sup>[24,27]</sup> (2) the high interfacial binding energy between Pt and transition metal carbides,<sup>[25,34]</sup> and (3) the low mobility of transition metal carbides anchoring the particle in place.<sup>[27]</sup> The high stability against dissolution and the resistance to sintering and restructuring results in a catalyst that shows almost no sign of degradation.

Finally, after verifying the exceptional structural stability of Pt/TaC, the electrocatalytic durability was assessed for the oxygen reduction reaction serving as a test reaction. To evaluate the performance of the ORR, the SA and MA of Pt<sub>2.6ML</sub>/TaC were determined via rotating disk electrode measurements and were compared to reference catalysts (Figure 4A, ECSA values in Figure S7). The given values are averaged over at least five independent measurements for each sample. The SA is with 1.1(0.2) mA cm<sup>-2</sup><sub>Pt</sub> lower than the initial SA of 10 nm large Pt<sub>3</sub>NiMo (1.7(0.3) mA cm<sup>-2</sup><sub>Pt</sub>) but double as high as 3 nm small pure Pt nanoparticles.<sup>[10]</sup> The SA of Pt<sub>2.6ML</sub>/TaC competes with the SA of a Pt black

catalyst (1.2 mA cm<sup>-2</sup><sub>Pt</sub>) consisting of 30 nm large Pt particles.<sup>[35]</sup> Due to the beneficial core-shell structuring, the MA is double as high (0.35(0.04) vs. 0.15 A mg<sup>-1</sup><sub>Pt</sub>) compared to Pt black and competes with state-of-the-art Pt<sub>3</sub>NiMo octahedra (0.46(0.04) A mg<sup>-1</sup><sub>Pt</sub>).

After determination of the beginning-of-life activity, Pt<sub>2.6ML</sub>/TaC was subjected to accelerated stress tests with 10,800 cycles between 0.4 and 1.0 V<sub>RHE</sub> (AST-1.0).<sup>[36,37]</sup> Pt<sub>2.6ML</sub>/TaC retained 74 and 69% of its initial SA and MA, respectively, which is slightly better compared to shaped controlled Pt<sub>3</sub>NiMo (71% of SA and 65% of MA). Together with an ECSA retention of 91% (Figure 4B), these results indicate high stability during fuel cell load.<sup>[38]</sup>

## 4 | CONCLUSION

To summarize, core-shell nanoparticles with a thin and inhomogeneous noble metal shell can be successfully sta-

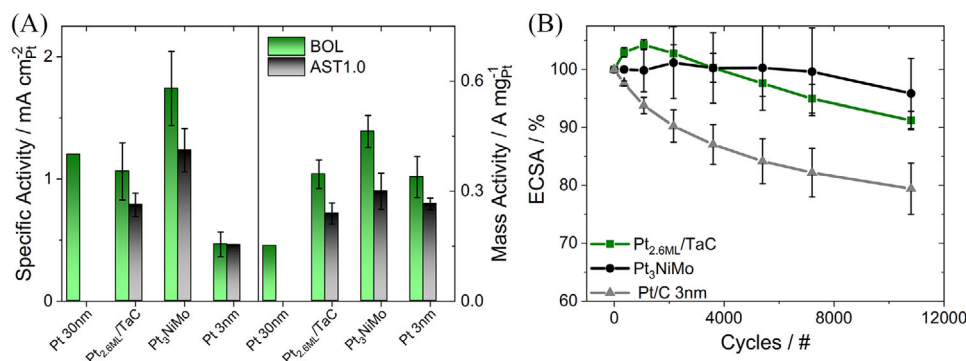


**FIGURE 4** A, Specific (left) and mass activity (right) of Pt<sub>2.6ML</sub>/TaC, 3 nm Pt/C (TKK), and 10 nm Pt<sub>3</sub>NiMo octahedra before accelerated stress tests, after 10,800 cycles between 0.4 and 1.0 V<sub>RHE</sub> (AST-1.0) at 1 V s<sup>-1</sup> in Ar-sat. 0.1 M HClO<sub>4</sub>. The reference value of Pt black (Pt 30 nm) was taken from reference.<sup>[35]</sup> B, The relative ECSA development of the three tested samples during AST-1.0

bilized by utilizing a passivating core material. Despite shell defects, Pt/TaC showed negligible degradation during the electrocatalytic oxygen reduction reaction up to 1.0 V<sub>RHE</sub>. The passivation of the TaC core decelerates the shell degradation, demonstrating the potential applicability of such ceramic core – noble metal shell architectures. Flow cell measurements with an on-line coupled inductively coupled plasma mass spectrometer revealed that core dissolution occurs only concomitantly to Pt dissolution, which is negligible under fuel cell load. Identical location transmission electron microscopy revealed that no restructuring occurs during an accelerated stress test consisting of 10,800 cycles due to the immiscibility of Pt and TaC and the high interfacial binding energy. This is in strong contrast to traditional Pt-transition metal alloys for which restructuring occurs during operation. Overall, our findings demonstrate a strong improvement in stability compared to state-of-the-art core-shell nanoparticles with non-noble cores and set another milestone on the path to the development of stable oxygen reduction catalysts with low Pt loading.

#### ACKNOWLEDGMENTS

M.L. and D.G. acknowledge the Federal Ministry of Education and Research (BMBF) in the framework of NanoMatFutur (SynKat) for financial support (project number 03XP0265). Z.W., J.S.K., and Y.R.-L. acknowledges the funding support from the Toyota Research Institute through the Accelerated Materials Design and Discovery program. M.H. and P.P. acknowledge the Federal Ministry for Economic Affairs and Energy (BMWi) of Germany in the framework of POREForm (project number 003ETB027G) for funding. Z.W., J.S.K., and Y.R.-L. acknowledge the Toyota Research Institute through the Accelerated Material Design and Discovery program.

Open access funding enabled and organized by Projekt DEAL.

#### CONFLICTS OF INTEREST

The authors declare no conflict of interest.

#### DATA AVAILABILITY STATEMENT

The data that support the findings of this study are available from the corresponding author upon reasonable request.

#### REFERENCES

1. A. N. Goldstein, C. M. Echer, A. P. Alivisatos, *Science* **1992**, 256, 1425.
2. M. Mamatkulov, J. S. Filhol, *J. Phys. Chem. C* **2013**, 117, 2334.
3. J. Kleis, J. Greeley, N. A. Romero, V. A. Morozov, H. Falsig, A. H. Larsen, J. Lu, J. J. Mortensen, M. Dułak, K. S. Thygesen, J. K. Nørskov, K. W. Jacobsen, *Catal. Lett.* **2011**, 141, 1067.
4. C. A. Johnson, *Surf. Sci.* **1965**, 3, 429.
5. S. Cherevko, N. Kulyk, K. J. J. Mayrhofer, *Nano Energy* **2016**, 29, 275.
6. M. Oezaslan, P. Strasser, *J. Power Sources* **2011**, 196, 5240.
7. X. Huang, Z. Zhao, L. Cao, Y. Chen, E. Zhu, Z. Lin, M. Li, A. Yan, A. Zettl, Y. M. Wang, X. Duan, T. Mueller, Y. Huang, *Science* **2015**, 348, 1230.
8. B. S. Mun, M. Watanabe, M. Rossi, V. Stamenkovic, N. M. Markovic, P. N. Ross, *J. Chem. Phys.* **2005**, 123, 204717.
9. M. Pourbaix, *Atlas of Electrochemical Equilibria in Aqueous Solutions*, NACE International Ceelcor, Houston, Brussels **1966**.
10. J. Knossalla, P. Paciok, D. Göhl, D. Jalalpoor, E. Pizzutilo, A. M. Mingers, M. Heggen, R. E. Dunin-Borkowski, K. J. J. Mayrhofer, F. Schüth, M. Ledendecker, *J. Am. Chem. Soc.* **2018**, 140, 15684.
11. R. Callejas-Tovar, C. A. Diaz, J. M. Martinez De La Hoz, P. B. Balbuena, *Electrochim. Acta* **2013**, 101, 326.
12. P. Mani, R. Srivastava, P. Strasser, *J. Phys. Chem. C* **2008**, 112, 2770.
13. K. Hartl, K. J. J. Mayrhofer, M. Lopez, D. Goia, M. Arenz, *Electrochem. Commun.* **2010**, 12, 1487.
14. A. L. Strickler, A. Jackson, T. F. Jaramillo, *ACS Energy Lett.* **2016**, 2, 244.
15. L. Yang, M. B. Vukmirovic, D. Su, K. Sasaki, J. A. Herron, M. Mavrikakis, S. Liao, R. R. Adzic, *J. Phys. Chem. C* **2013**, 117, 1748.

16. X. Wang, S.-I. Choi, L. T. Roling, M. Luo, C. Ma, L. Zhang, M. Chi, J. Liu, Z. Xie, J. A. Herron, M. Mavrikakis, Y. Xia, *Nat. Commun.* **2015**, *6*, 1.
17. J. Zhang, M. B. Vukmirovic, Y. Xu, M. Mavrikakis, R. R. Adzic, *Angew. Chemie - Int. Ed.* **2005**, *44*, 2132.
18. A. S. Nair, B. Pathak, *J. Phys. Chem. C* **2019**, *123*, 3634.
19. P. Strasser, S. Koh, T. Anniyev, J. Greeley, K. More, C. Yu, Z. Liu, S. Kaya, D. Nordlund, H. Ogasawara, M. F. Toney, A. Nilsson, *Nat. Chem.* **2010**, *2*, 454.
20. P. P. Lopes, D. Li, H. Lv, C. Wang, D. Tripkovic, Y. Zhu, R. Schimmenti, H. Daimon, Y. Kang, J. Snyder, N. Becknell, K. L. More, D. Strmcnik, N. M. Markovic, M. Mavrikakis, V. R. Stamenkovic, *Nat. Mater.* **2020**, *19*, 1207.
21. K. Sasaki, H. Naohara, Y. Cai, Y. M. Choi, P. Liu, M. B. Vukmirovic, J. X. Wang, R. R. Adzic, *Angew. Chemie - Int. Ed.* **2010**, *49*, 8602.
22. A. Kongkanand, N. P. Subramanian, Y. Yu, Z. Liu, H. Igarashi, D. A. Muller, *ACS Catal.* **2016**, *6*, 1578.
23. D. Göhl, H. Rueß, S. Schlicht, A. Vogel, M. Rohwerder, K. J. J. Mayrhofer, J. Bachmann, Y. Roman-Leshkov, J. M. Schneider, M. Ledendecker, *ChemElectroChem* **2020**, *7*, 2404.
24. S. T. Oyama, *The Chemistry of Transition Metal Carbides and Nitrides*, Blackie Academic and Professional, Glasgow, UK **1996**.
25. C. H. Hendon, S. T. Hunt, M. Milina, K. T. Butler, A. Walsh, Y. Román-Leshkov, *J. Phys. Chem. Lett.* **2016**, *7*, 4475.
26. D. Göhl, H. Rueß, M. Pander, A. R. Zeradjanin, K. J. J. Mayrhofer, J. M. Schneider, A. Erbe, M. Ledendecker, *J. Electrochem. Soc.* **2020**, *167*, 021501.
27. S. T. Hunt, M. Milina, A. C. Alba-Rubio, C. H. Hendon, J. A. Dumesic, Y. Román-Leshkov, *Science*. **2016**, *352*, 974.
28. Z. Wang, J. S. Kang, D. Göhl, P. Paciok, K. J. J. Mayrhofer, M. Heggen, R. E. Dunin-Borkowski, Y. Shao-Horn, M. Ledendecker, Y. Román-Leshkov, *Prep. n.d.n.d.*
29. P. Scherrer, *Nachrichten von der Gesellschaft der Wissenschaften zu Göttingen* **1918**, *2*, 98.
30. H. Natter, M. Schmelzer, M.-S. Löffler, C. E. Krill, A. Fitch, R. Hempelmann, *J. Phys. Chem. B* **2000**, *104*, 2467.
31. S. O. Klemm, A. A. Topalov, C. A. Laska, K. J. J. Mayrhofer, *Electrochem. Commun.* **2011**, *13*, 1533.
32. A. A. Topalov, S. Cherevko, A. R. Zeradjanin, J. C. Meier, I. Katsounaros, K. J. J. Mayrhofer, *Chem. Sci.* **2014**, *5*, 631.
33. D. Göhl, A. Garg, P. Paciok, K. J. J. Mayrhofer, M. Heggen, Y. Shao-horn, R. E. Dunin-borkowski, Y. Román-leshkov, M. Ledendecker, *Nat. Mater.* **2020**, *19*, 287.
34. S. T. Hunt, Y. Román-Leshkov, *Acc. Chem. Res.* **2018**, *51*, 1054.
35. M. Nesselberger, S. Ashton, J. C. Meier, I. Katsounaros, K. J. J. Mayrhofer, M. Arenz, *J. Am. Chem. Soc.* **2011**, *133*, 17428.
36. H. Tang, Z. Qi, M. Ramani, J. F. Elter, *J. Power Sources* **2006**, *158*, 1306.
37. C. A. Reiser, L. Bregoli, T. W. Patterson, J. S. Yi, J. D. Yang, M. L. Perry, T. D. Jarvi, *Electrochem. Solid-State Lett.* **2005**, *8*, A273.
38. Office of Energy Efficiency & Renewable Energy, *Fuel Cell Technologies Office Multi-Year Research, Development, and Demonstration Plan*, Section 3.4 Fuel Cells, **2016**.

## SUPPORTING INFORMATION

Additional supporting information can be found online in the Supporting Information section at the end of this article.

**How to cite this article:** D. Göhl, P. Paciok, Z. Wang, J.S. Kang, M. Heggen, K.J.J. Mayrhofer, Y. Román-Leshkov, M. Ledendecker, *Nano Select*. **2023**, *1*. <https://doi.org/10.1002/nano.202200240>